Author's post-print version

CFD Modeling of High Speed Liquid Jets From an Air-Powered Needle-Free Injection System

Haruka Nakayama

Department of Mechanical and Industrial Engineering, Concordia University
Montreal, Quebec, H3G 1M8, Canada

Rocco Portaro

Department of Mechanical and Industrial Engineering, Concordia University
Montreal, Quebec, H3G 1M8, Canada

Charles Basenga Kiyanda

Department of Mechanical and Industrial Engineering, Concordia University
Montreal, Quebec, H3G 1M8, Canada

Hoi Dick Ng

Department of Mechanical and Industrial Engineering, Concordia University
Montreal, Quebec, H3G 1M8, Canada
hoing@encs.concordia.ca

A liquid jet injector is a biomedical device intended for drug delivery. Medication is delivered through a fluid stream that penetrates the skin. This small diameter liquid stream is created by a piston forcing a fluid column through a nozzle, these devices can be powered by springs or compressed gas. In this study, a CFD simulation is carried out to investigate the fluid mechanics and performance of needle free injectors powered specifically by compressed air. The motion of the internal mechanisms of the injector which propel a liquid jet through an orifice is simulated by the moving boundary method and the fluid dynamics is modeled using LES/VOF techniques. In this paper, numerical results are discussed by comparing the fluid stagnation pressures of the liquid jet with previously published experimental measurement obtained using a custom-built prototype of the air-powered needle free liquid injector. Performance plots as a function of various injector parameters are constructed and explained.

Keywords: CFD simulation; needle free liquid injection; air-powered system; stagnation pressure; drug delivery; OpenFOAM.

1991 Mathematics Subject Classification: 22E46, 53C35, 57S20

1. Introduction

Drug delivery using conventional hypodermic needles has long remained one of the only means available to healthcare professionals to effectively administer a broad

2   *Nakayama et al.*

range of medication. Nevertheless, this traditional practice is accompanied by many disadvantages; vaccination by a needle-syringe is troublesome for many children since it causes pain, scare and additional stress. In insulin delivery, traditional injections using needle-syringes is often a burden especially for beginners and children. In animal-production industries, there is also a need for improvement in vaccines and their delivery system in terms of cost, safety compliance as well as minimizing animal stress. To address the above issues, needle-free, liquid-jet injections have long been considered as an alternate technique to effectively deliver medication to the different layers of skin for humans and animals other than traditional drug delivery using hypodermic needles [1,2]. The liquid jet injector delivers medication by a force generated from a power source which is imparted on a cylinder and forces a column of fluid containing the drug through a nozzle. The liquid exits as a high-speed small diameter liquid jet of sufficient pressure penetrating the skin and delivering the appropriate amount of medication. Typical design of needle-free injectors generally produces jet exit velocities greater than 100 m/s and diameters ranging from 100 to 360 μm with an initial pressure change of 27.5 MPa within 0.5 ms [1,3]. The volume of injection ranges from 0.1 to 1 ml with a skin penetration depth of up to 10 mm. Figure 1 illustrates the process of liquid jet injection into a ballistic gel and to air from a custom-built air-powered needle-free injector prototype [4].

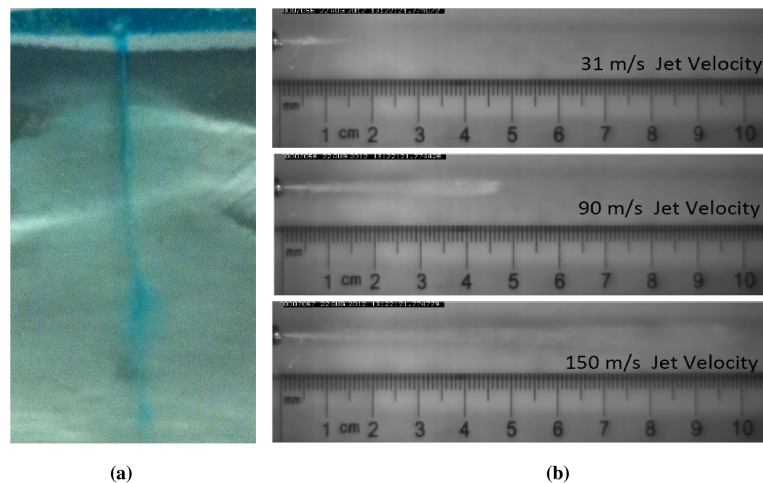(a)   (b)

Fig. 1.   Photographs showing a) the jet penetration into a ballistic gel; and b) the liquid jet exiting the injector nozzle (Portaro and Ng, 2013)

In order to alleviate the problems with the early use of liquid jet injectors such as pain, bruising, hematomas, incomplete delivery of medication, excessive penetration and cross contamination [5,6,7], much research has been conducted on improving their performance by analyzing the fluid mechanics of jet injection. A number of

research papers, notably by Schramm and Mitragotri (2002)[8], Schramm-Baxter and Mitragotri (2004)[9,10], Schramm-Baxter et al. (2004)[11], etc., performed detailed experiments and reported the dependence of fluid jet penetration into human skin on different injector parameters. Furthermore, the development of simple analytical models to simulate the skin fracture and medicine delivery, as well as to predict the jet pressure and velocity distribution are also emerging and serve to compliment experimental studies (e.g., Baker and Sanders, 1999[12]; Shergold et al. 2006 [13]; Chen et al. 2010)[14].

Although there exists a number of different types of needle-free liquid jet injectors that can be classified by their power source such as, spring-loaded devices[4,10], Lorentz-force actuators[15,16,17] and piezoelectric actuators[18], this study focuses on the development and analysis of the air-powered liquid jet injectors using Computational Fluid Dynamics (CFD). Studies demonstrate that the majority of commercially available injectors are gas/air powered units,[19], however there is no indication of an engineering model that prescribes the performance characteristics of this particular type of injector. Although a number of simulations on needle-free powder injection systems can be found in literature [20,21,22,23,24], the use of CFD to describe needle-free liquid jet injections is rather scarce. Perhaps, one of the most relevant studies is that of [25] where CFD simulation is performed to study the spring-powered needle-free injection into the air. Their CFD model consists of a two-fluid formulation using the volume-of-fraction VOF approach and turbulence is modeled using standard k-ϵ model. A limited number of CFD results were given, such as the jet average velocity and jet power. These results were then compared with their experimental counterparts. The main goal of this paper is therefore to develop a numerical CFD model with further improvements which can accurately capture the injection fluid dynamic behavior of the high speed jet emanating from an air-powered needle-free injector. The paper compares the numerical results with experimental measurements obtained using a prototype injector with identical geometry. The experimental prototype functions in a very similar fashion and produces jets of similar geometry and velocities as the vast majority of commercially available units. A parametric study using the developed numerical model is also carried out to analyze the influence of various injector parameters such as driver pressure, injection chamber length and volume as well as nozzle sizes, on the jet injection process.The stagnation pressure evolution produced at the injector nozzle, which is broken down into a peak pressure as well as a time-averaged and space-averaged pressure, is the key metric used to analyze the behavior of different injector parameters.

2. Numerical Model

In this study, CFD is applied to the analysis of needle free jet injectors. The research mainly addresses the fluid dynamics of the high speed jet emanating from an air-powered needle-free injector and analyzes the effect of injector parameters on the jet injection process. Numerical simulations of the high-speed liquid jet gen-

4   *Nakayama et al.*

eration process from the needle-free injector are carried out using the OpenFOAM CFD software package[26]. The geometrical model is equivalent to a custom-built experimental prototype[4] as shown in fig. 2, which consists of a driver chamber containing high-pressure gas, a moving piston with O-rings, an injection chamber containing the liquid and an orifice-type nozzle. High-speed jets are emitted into the air through the orifice. It is important to note that the driver chamber for the experimental prototype consists of a constant air-mass system. Once the driver chamber is pressurized, a butterfly valve at the inlet is used to prevent further air flow from entering the chamber while the injection is delivered. Some important dimension and operating characteristics of the experimental prototype injector are summarized in table 1.
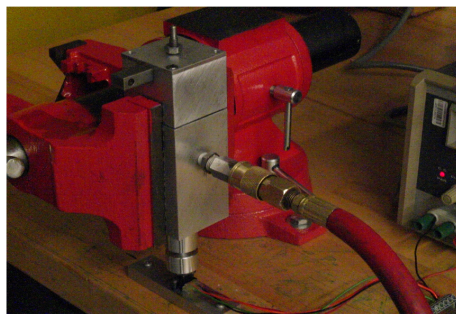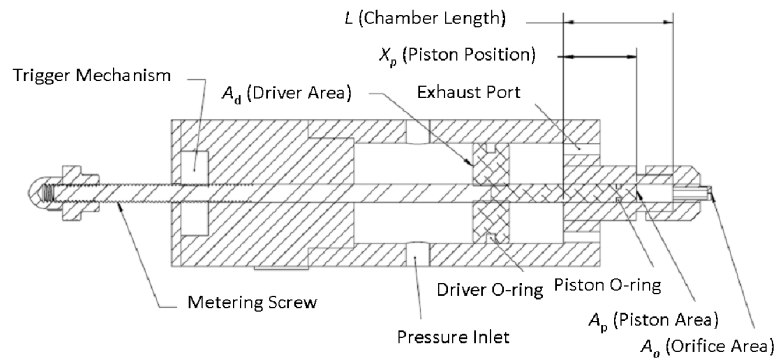

Fig. 2.   A photograph showing the experimental prototype of an air-powered needle-free injector (Portaro and Ng, 2013)

The injection chamber, the orifice and the atmospheric region are modeled in this simulation study as an axi-symmetric geometry as shown in fig. 3. The piston, driver chamber, and O-ring resistance are modeled as a two-dimensional moving wall located at the left hand boundary, with a dynamic model that mirrors the analysis in Portaro and Ng (2013)[27].

Table 1.   Key dimensions and operating characteristics of the injector.

Injector parameters	
Nozzle diameter	$100 - 260$ μm
Driver pressure	$3 - 10$ Bar
Injection volume	$0 - 1.2$ ml
Piston diameter	6.35 mm
Driver diameter	38.1 mm
m_p (mass of piston-driver assembly)	80 g

The two models – the analytical differential equation representing the injection piston, and the CFD description of the injection fluid and atmosphere – are coupled through the pressure at the piston face, i.e. $P(t)$ in equations 1 and 5, derived in the following section.

2.1. *Moving Wall Model*

In order to physically model the injection process, the liquid in the injection chamber is initially impacted abruptly by the moving grid boundary to mimic the in-
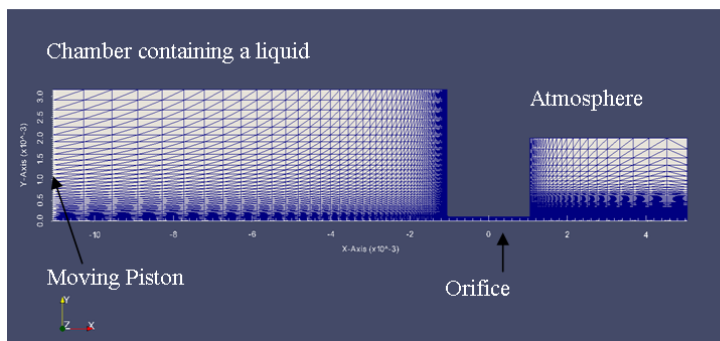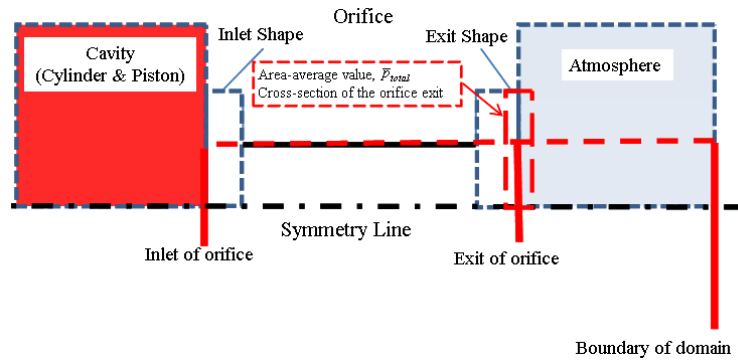

Fig. 3.   The layout of the computational domain.

jector piston which is driven by the driver chamber air pressure. As a result of the injector piston impacting the fluid at high speed, a liquid jet is emitted into the atmospheric region through a nozzle. The moving boundary position/velocity is obtained by solving an ordinary differential equation derived from a force balance at each computational time step. For the numerical modeling of the piston motion, the following assumptions are introduced:

(1) The piston is a solid body (no-deformation occurs) and its mass is constant;
(2) The thickness of the piston is neglected (assumed as 2-dimentional object);
(3) Back leakage of liquid through the gap between the O-ring and the inner surface of the cylinder is neglected;
(4) Gravitational force is neglected.

During the injection process, the piston is pushed by the high-pressure gas contained in the driver part and impacts the liquid inside the chamber. However, the injection chamber liquid generates a backward force as the fluid is being compressed. Furthermore, the friction force between the O-rings and the inner surface of the cylinder should be taken into consideration during the motion. As a result, the piston motion is determined as a summation of the driver force by the gas pressure inside the driver chamber, the pressure of the injection fluid, and the O-ring friction force[27,28], i.e.,

$$\frac{d^2 x_p}{dt^2} = \frac{F_D(t)}{m_p} - \frac{A_p p(t)}{m_p} - \frac{F_f(t)}{m_p} \tag{1}$$

where F_D and F_f are the driving force and frictional force, and $p(t)$ is the fluid pressure on the piston boundary and A_p and m_p are the piston surface area and mass, respectively. The piston is initially at rest, such that at $t = 0$, $x_p = 0$, and $dx/dt = 0$. For an air-powered injection system, the driving force F_D which moves the plunger forward is produced by pressurizing the driver chamber. The pressure within the driver chamber can be modeled by using the ideal gas law and the initial driver chamber pressure. The pressure within the chamber can be computed as a function of driver displacement, i.e.:

$$p_d = \frac{mRT}{V_D(t)} \tag{2}$$

with

$$V_D(t) = (L_0 + x_p(t)) A_D \tag{3}$$

Equation 3 clearly shows this model represents a case where the injection chamber contains a fixed amount of gas, such as in a disposable air-powered injection device. The case of reservoir or pressurized line fed injectors would be handled by assuming $p_d = $ constant. As the driving force begins to move the piston forward, there is resistance created by the atmospheric pressure, pa, acting on the opposite side of the driver face. This force can be assumed to remain constant throughout the

injection process and is simply the product of atmospheric pressure and the driver area. This gives:

$$F_D(t) = A_D \left(\frac{mRT}{V_D(t) - p_a} \right) \tag{4}$$

The frictional forces within the mechanism counteract and damp the movement of the driver/piston assembly. The friction is caused by the O-ring seals which make contact and rub against the inner walls of both the driver chamber and the injection chamber. In order to model the O-ring friction it must be broken down into two components: the first consists of the friction force caused by the compression fit of the O-ring into its housing, the second is a result of the thin fluid film which is generated in the clearance gap between the two components that the O-ring must seal. The forces caused by the compression of the O-ring, in the barrel of the injector is also dependent on the force generated by the pressure of the fluid. Consequently, the two major forces causing O-ring friction must be coupled in order to accurately model friction. Using the concepts from tribology[27,28], the fluid pressure imposed on the O-ring can be approximated by applying the Reynolds equations.

$$\bar{p}_{\mathrm{O-ring}} \approx \frac{1}{2} \frac{6\mu U(t)}{h^2} \frac{d}{2} + p(t) \tag{5}$$

As a result of knowing the pressure imposed by the fluid on the O-ring seal, the resisting force caused by this pressure is simply the area of exposed O-ring multiplied by the corresponding pressure, i.e.,

$$F_{\mathrm{fluid}} = \bar{p}_{\mathrm{O-ring}} \pi D h \tag{6}$$

The amount of compression fit related force, κ, as a function of load that an O-ring will produce can be found from empirical charts[29]. The force produced by the compression of an O-ring depends both on the O-ring cross section and durmometer, for the three O-rings in the current model values of 96 N, 5.2 N and 3.5 N are used. In addition to the force caused by the compression of the O-ring into the barrel of the injector, it is also necessary to take into consideration the transfer of forces caused by the fluid pressure on the O-ring. The fluid pressure that acts on the seal also serves to further increase the compression loading. Studies conducted by Guang and Wang[30] demonstrate that the transfer coefficient between the fluid pressure acting on a seal in relation to the increase of compression force of the O-ring can be estimated at unity. In other words, the pressure contained within the thin film acting on the seal almost entirely serves to increase the amount of compression forces on the sealing surfaces. Knowing that the coefficient of friction between aluminum and nitrile rubber is $\alpha = 0.2$ (Chen et al. 2011[28]; Portaro and Ng, 2013[27]), the resisting force encountered by individual O-ring seals in the injector can be completely described through Eq. 7:

$$F_f(t)_{\mathrm{O-ring}} = \left(\alpha \bar{p}_{\mathrm{O-ring}}(t) \pi D b \right) + \left(\bar{p}_{\mathrm{O-ring}}(t) \pi D h \right) + \alpha \kappa \tag{7}$$

8   *Nakayama et al.*

During computation, the piston position/velocity as a function of time can therefore be obtained by solving Eq. 1 together with Eq. 2 to Eq. 7, simultaneously with the CFD solution. These equations govern the equation of motion of the piston and are incorporated into a class in OpenFOAM. Figure 4 illustrates the behavior of the piston from sample simulations showing the maximum piston velocity occurring at the very beginning before the frictional forces and fluid forces can damp the motion. The oscillatory nature of the piston displacement is expected as the system is underdamped. In the limiting case where there is no frictional loss (i.e. no O-ring force), the injection fluid pressure must exceed the driver chamber pressure for the piston to slow-down. Hence, the piston location always reaches a local maximum when there is a net force backwards and inversely for local piston location minima. The O-ring frictional force is related to the magnitude of the piston velocity and cannot overdamp the system. Using the piston position/velocity as boundary conditions, a Laplace equation related to the mesh motion, as illustrated in fig. 5, is solved to determine a new mesh using the dynamic mesh classes in OpenFOAM, i.e.,

$$\nabla \cdot (\gamma \nabla u_m) = 0 \tag{8}$$

where γ can be considered constant or variable diffusivity and u_m is mesh motion velocity or mesh point displacement.
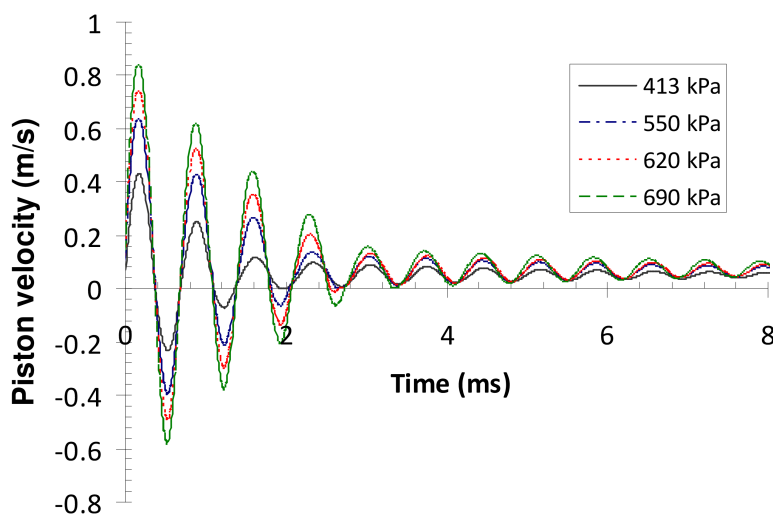

Fig. 4.   Simulation of the driver piston velocity for four different driver pressures.

2.2. *Fluid CFD Model Description*

Physical dimensions and average gird size for each domain are summarized in table 2. It is noted that average cell size given in the table is for the base mesh case and the grid is in fact refined near the orifice inlet/exit to capture steep gradient of pressure, velocity and volume fraction of liquid. The structured mesh is gener-
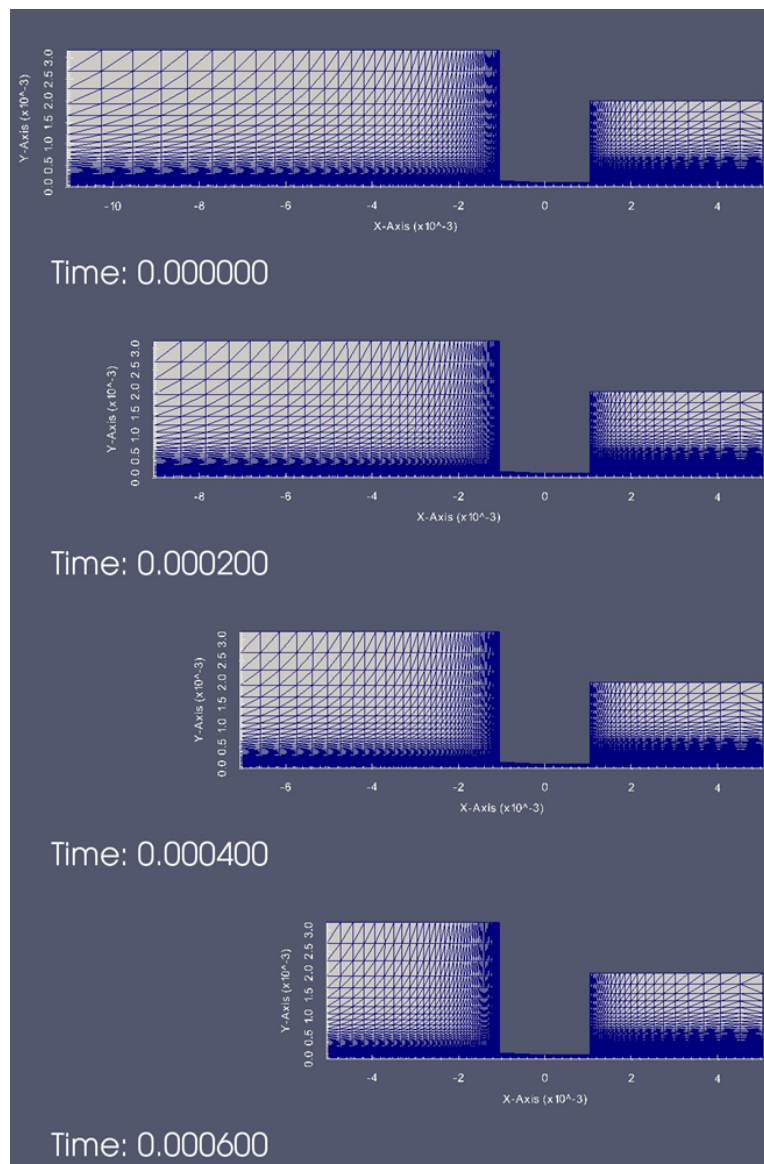

Fig. 5.   An example showing the 1-D piston motion and the dynamic mesh.

ated by a built-in utility in OpenFOAM. The domain boundaries have zero gradient Neumann conditions for the liquid volume fraction, the sub grid scale (SGS) stress, pressure, temperature and non-slip condition on velocity. The Dirichlet condition is applied for the SGS turbulent energy and a fixed total pressure (i.e., 101,325 Pa) is imposed on the atmosphere exit boundaries.

Table 2.   Physical dimensions of the computational domain and the base mesh size (unit: mm).

Domain name	radius (y-coordinate)		Length (x-coordinate)	
	Dimension	Average cell size	Dimension	Average cell size
Chamber	3.175	0.064	10	0.20
Orifice	0.1	0.001	2.1	0.04
Atmosphere	2	0.033	4	0.16

For the fluid properties, the two fluid phases are initially divided into a liquid phase consisting of water in the chamber/orifice and a gas phase (air) in the atmosphere region. The gas density is simply specified by using the ideal gas formula for the air to cope with the compressible flow field. In the injection chamber and orifice, it is more complicated to specify the water as a compressible liquid, therefore variable density is specified with compressibility. In equation 9, the variables p and ρ are the liquid pressure and density, respectively. The compressibility ψ and the bulk modulus of elasticity of the liquid B are a function of pressure and temperature. These are updated after solving the energy equation (Eq. 10 at each time step. Then, the density is updated in the linearized equation (Eq. 11 during the simulation. Subscripts $_0$ and $_1$ denote the respective quantity at the initial and current time.

$$\frac{\partial \rho}{\partial p} = \frac{\rho}{B} = \psi, \tag{9}$$

$$\frac{\partial (\rho T)}{\partial t} + \nabla \cdot (\rho U T) - \nabla \cdot \left(\frac{k}{C_v} \right) \nabla T = \frac{p}{C_v} \nabla \cdot U, \tag{10}$$

$$\rho_1 \approx \rho_0 + \psi (p_1 - p_0). \tag{11}$$

The Volume-of-Fluid (VOF) method is then used to update the position of the interface between two phases by computing the transport equation for the liquid volume fraction as the indicator function to locate the interface.

$$\frac{\partial (\rho \alpha)}{\partial t} + \nabla \cdot (\rho U \alpha) = 0 \tag{12}$$

with the liquid-phase volume fraction α,

$$\alpha = \begin{cases} 0 & \text{for a cell inside the gas,} \\ 0 < \alpha < 1 & \text{for a cell inside the transitional region,} \\ 1 & \text{for a cell contained completely in the liquid.} \end{cases} \tag{13}$$

By determining the volume fraction α, the local properties of fluid are computed based on the single state of each phase, i.e., the local density, ρ, and the local viscosity, μ of the fluid are interpolated across the interface as follows:

$$\rho = \alpha \rho_l + (1 - \alpha) \rho_g, \tag{14}$$

$$\mu = \alpha \mu_l + (1 - \alpha) \mu_g. \tag{15}$$

where the subscripts $_l$ and $_g$ denote the liquid- and gas-phases, respectively. For the present simulations, the properties of the different fluids are given in Table 3.

Table 3.   Physical properties for the two phases at room temperature.

Phase	Kinematic Viscosity ν[m^2/s]	Density ρ [kg/m^3]	Compressibility ψ[s^2/m^2]	Volumetric Heat Capacity C_v [J/m^{3}K]	Thermal Conductivity k [W/mK]
Water (liquid)	8.714x10^{-7}	9.970x10^2	4.440x10^{-7}	4.180x10^3	6.130x10^{-1}
Air (gas)	1.557x10^{-5}	1.19	1.160x10^{-5}	7.210x10^2	2.620x10^{-2}

The governing equations of the phenomenon consist of the transport equations for conservation of mass and momentum of a two-phase flow system, comprised of two immiscible, compressible Newtonian fluids, including surface tension[26]. Finite volume method with 2nd order accuracy is used to discretize the governing conservation equations. Large Eddy Simulation (LES) is applied for turbulence model. The solver used to compute the solutions of the discretizing equations follows the PISO-SIMPLE (PIMPLE) algorithm[31,32]. In the unsteady flow solution, the time step size, Δt, of 1x10^{-8} $\sim$ 5x10^{-9} s is selected to obtain stable solutions. In OpenFOAM, the combination of compressibleInterFoam and oneEgEddy realizes the above models as multi-phase Navier-Stokes solver (thus simulating viscous fluids in the injection chamber and the air) and LES model respectively.

3. Results and Discussions

The dynamic characteristics of the high-speed liquid jet emitted from the injector nozzle can be illustrated qualitatively first by the phase fraction plots shown in Fig. 6. In this figure, the liquid jet structure is computed with a fine mesh (i.e., with the smallest level $\Delta x = 0.01$ mm and $\Delta r = 2.5$x10^{-4} mm) to reveal detailed features of the liquid jet. These images from CFD provide a clear depiction of jet roll-up during the initial start-up of the injection process. As the jet emerges from the nozzle the re-circulation on the corner causes a blunt shape of the leading front of the jet. The CFD solution also demonstrates that part of the jet starts to atomize generating a spray. Nevertheless, it is possible to conclude that at initial stages the overall jet divergence is minimal. The diameter of the jet is relatively close to the nozzle diameter during the continuous injection process. The pain and bruising

12   *Nakayama et al.*

associated with medical injection devices is most often addressed by reducing the size of the injector, for example by using an array of micro-needles instead of a single larger needle. It is promising that the jet enlargement due to turbulence in the needle-free injector is minimal, as jet enlargement would likely increase the bruising and pain associated with injection.
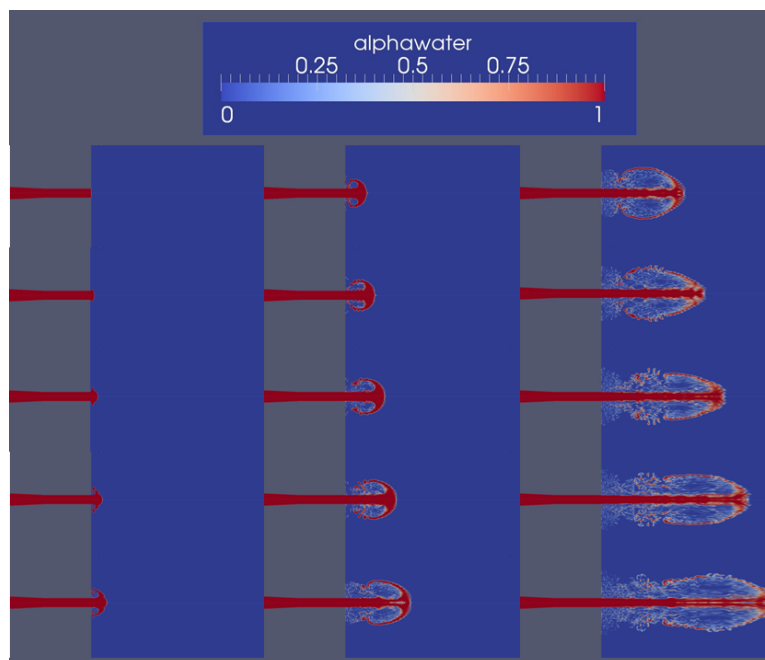

Fig. 6.   CFD results showing the time evolution of the jet emitted from the 200 μm injector nozzle and driven by a 413 kPa driver pressure.

For a quantitative assessment of the numerical model, it is possible to extract some key variables from the simulations and compare with available experimental measurement. Among different injection performance indicators the stagnation pressure is one of the fundamental measurements as it is the key parameter which determines the force at which the liquid jet will penetrate the skin and deliver a successful injection[28]. To verify the numerical solutions, the computed, space-averaged (over the jet area) jet stagnation pressures are compared with experimental results. From the CFD solutions, the stagnation pressure can be determined by adding both static and dynamic pressures. Unless specified, the numerical result is taken at the exit of the orifice, see fig. 3. It is worth noting that experimental stagnation pressures were measured using a force transducer Honeywell (Model FSG15N1A). This piezoelectric transducer originally developed to measure air jets was adapted to provide a cost effective means of measuring small forces from the water jets under

investigation. In order to ensure proper force measurements a minimum standoff distance of 3 mm was used. This distance mitigates the effects of splash back and over spray which cause noise and inaccurate force profiles. It is important to note that this transducer has been used successfully by other research groups as detailed in Chen et al. 2011[28] to validate analytical models such as that of Baker and Sanders, 1999[12]. The stagnation pressure is subsequently computed with the force readings obtained by simply dividing them by the area of the jet, which is assumed to be equivalent to the nozzle size. Comparison is first made for an injector with a 200 μm nozzle driven at 413 kPa and a sample result is shown in fig. 7. In general, the CFD simulation demonstrates a similar behavior as that observed from the experiment. A pressure peak first occurs within the first millisecond and the pressure then oscillates about a mean injection pressure. This peak is often believed to be responsible for the formation of a fracture in the skin and the subsequent average delivery pressure determines the depth at which the medication is delivered[33]. The magnitude of the peak pressure and average pressure obtained from CFD and experimental measurement also agree well with each other within the experimental limitation. A possible explanation for the discrepancy stems from the degree of accuracy and sensitivity of the force transducer and the correct estimate of the jet area/location for the conversion to stagnation pressure. In fact, for the sensitivity of the probe a variation of 2 MPa represents approximately a force variation of 0.0264 N (2.693 g). The transducer's range varies from 0-1500 g. Hence, a difference of 2 MPa would correspond to 0.18% of the transducers range, and the slight difference between CFD and experiments can likely be attributed to the inaccuracies of the force transducer. It is worth noting that if the computed stagnation pressure at the centerline is used for comparison instead of the space-averaged data shown in fig. 7, a much better result can be obtained, as shown in fig. 8, although the asymptotic value of the stagnation pressure is too high. Furthermore, the rise time to peak pressure and subsequent stabilization to the average pressure occur very rapidly. On the modeling side, the limitation of the O-ring friction model is another possible source for discrepancy relating to the greater divergence from the CFD solution of peak pressure, as O-ring friction is difficult to model because of its variability with pressure. The numerical model also assumes an axisymmetric solution, suppressing any angular variation that would lead to 3-dimensional effects.

However to verify the difference is not due to the numerical grid resolution, a mesh dependency test is performed for the same 200 μm nozzle case shown in fig. 7 and 8. The value of the peak stagnation pressure (occurring at about $t = 0.2$ ms in figs 7 and 8) and the average pressure are reported in fig. 9 for both the space-averaged, and centerline results. The resolution study confirms that the (base) mesh size used in fig. 7 and fig. 8 is sufficient for convergence of both the computed peak and average stagnation pressures. Taking all these influences into account, the numerical CFD model is valid in predicting the performance of the injector in terms of the peak and average stagnation pressures, given the injector geometry and driver

14   *Nakayama et al.*

pressure.

The numerical result of space-averaged velocity from CFD is also shown in fig. 10. It can be observed that the peak velocity obtained from the CFD simulation also corresponds well with the 150–200 m/s range[2]. For comparison, the jet velocity as the jet exits the orifices, converted from the experimentally measured stagnation pressure using the Bernoulli equation with constant water density, is also shown in the plot and a good agreement can also be seen.

A parametric study of two main injector characteristics, i.e., driver pressure
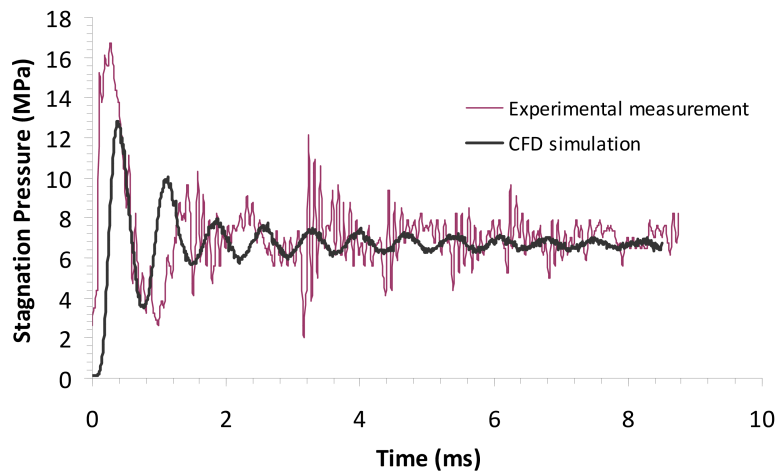
Fig. 7.   The time evolution of stagnation pressure from the CFD simulation (space averaged value) and experimental measurement for 200 μm nozzle at 413 kPa driver pressure.
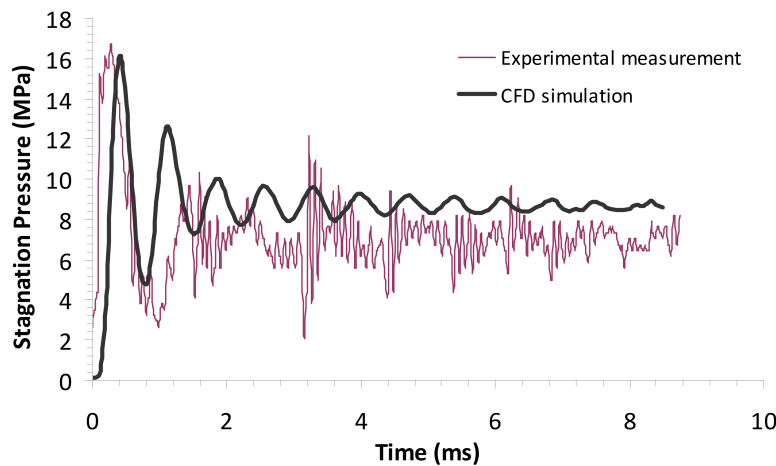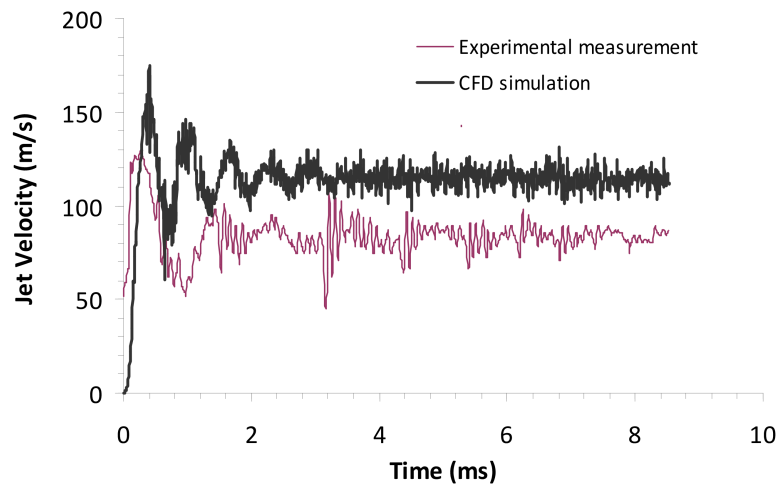

Fig. 8.   The time evolution of stagnation pressure from the CFD simulation (centerline value) and experimental measurement for 200 μm nozzle at 413 kPa driver pressure.

and nozzle size, is performed and summarized in fig. 11 and fig. 12. Simulations were performed for five different nozzles operating at four different driver pressures of 413, 550, 620 and 690 kPa. Also shown in these figures are the experimental data with 95% confidence interval error bars for comparison.

Figure 11 illustrates the peak stagnation pressure variation as a function of driver pressure for different nozzle sizes. A visual examination of both CFD and experimental data suggests a linear increase in the peak pressure as the driver pressure is increased from 413 to 690 kPa. Indeed, the least square linear regressions
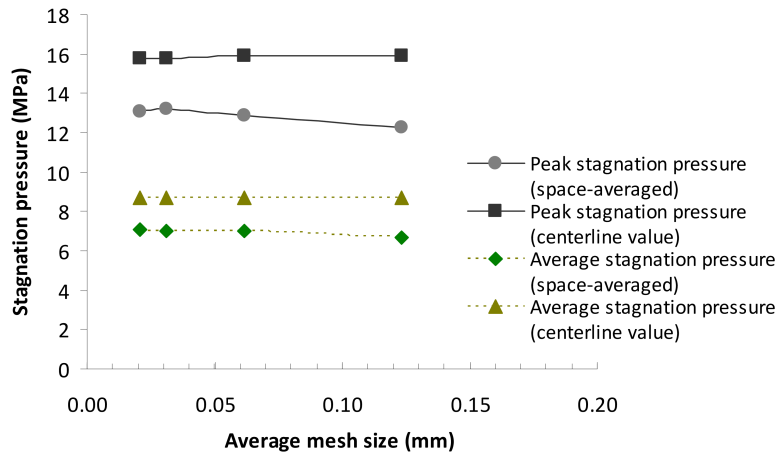
Fig. 9.   Resolution test showing the mesh dependency of the computed stagnation pressures.

Fig. 10.   The time evolution of jet velocity from the CFD simulation (space averaged value) and experimental measurement for 200 μm nozzle at 413 kPa driver pressure.

16   *Nakayama et al.*

obtained for both results have the coefficient of determination R^2 values above 0.80 (0.9968 for CFD space-averaged, 0.9871 for CFD centerline and 0.8396 for the experiments). In addition, the numerical results from the CFD model agree very well with the experimental data again by taking into account different experimental limitations as previously discussed.

Similarly, the average stagnation pressure after the pressure peak was also analyzed. Figure 12 demonstrates the variation of average injection pressure after the pressure peak, as a function of driver pressure for varying nozzle diameters. The CFD solutions show a linear increase in stagnation pressure as the driver pressure increases within the operating range, and this agrees with the trend from the exper-
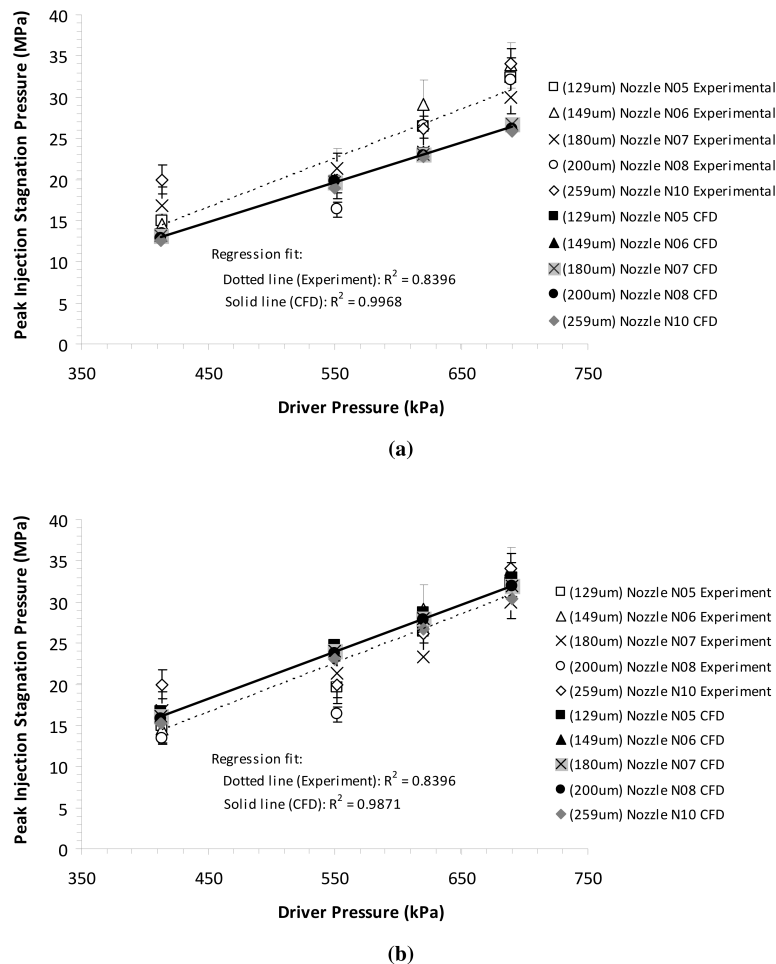

(a)

(b)

Fig. 11.   Peak stagnation pressure as a function driver pressure. a) space-averaged CFD value; and b) centerline CFD value.

imental measurement. The R^2 values from the least-square regression are 0.8006, 0.9984 (space-averaged) and 0.9996 (center-line), respectively, for the experimental and CFD correlations. However, it appears that the experimental data for average pressure is slightly higher than the predicted values obtained using the CFD model. Nevertheless this variation is still acceptable given that the force it represents is only a small fraction of the force transducer's range.

From fig. 11 and fig. 12, it can be observed from CFD simulations and equivalently depicted from experimental results that there is no significant variation
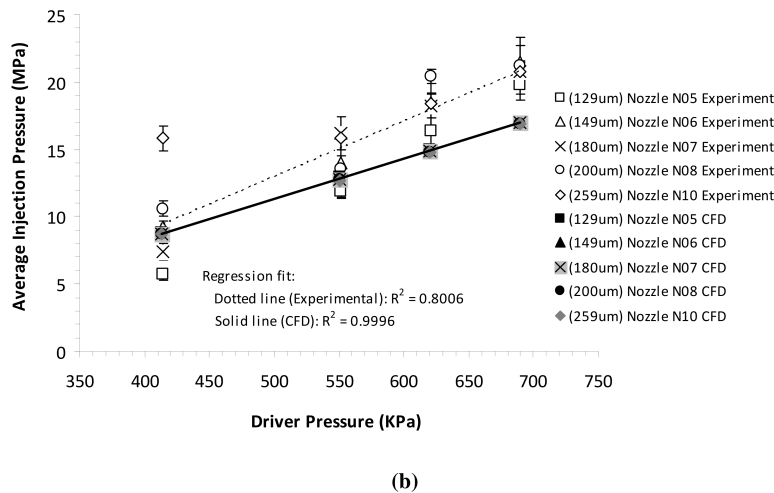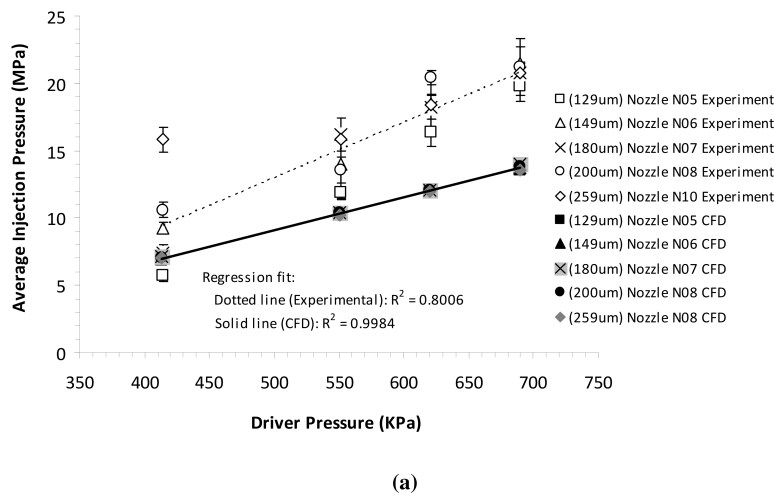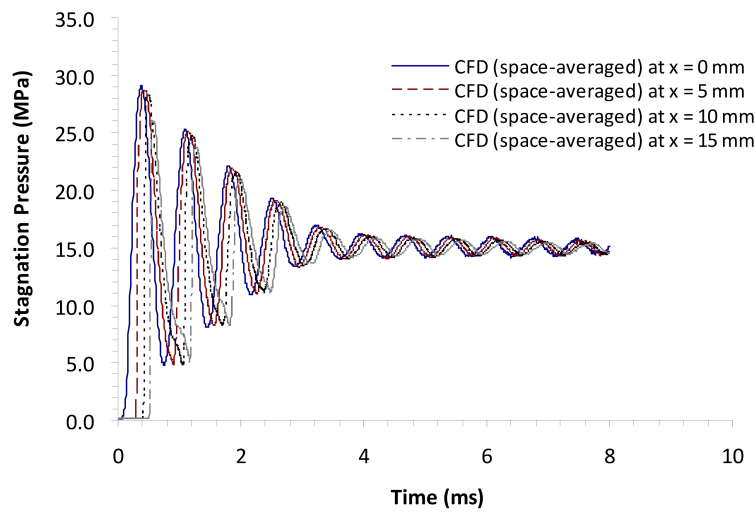

(a)

(b)

Fig. 12. Average stagnation pressure as a function driver pressure. a) space-averaged CFD value; and b) centerline CFD value.

between the stagnation pressures values obtained using different nozzle sizes at the same driver pressure. These pressure values with different nozzle sizes (particularly from the CFD simulations) are very close to each other. In this numerical study, th eobtained CFD results confirm our previous conjecture that the nozzle diameters do not have a large impact on the resulting stagnation pressures[27]. The weak dependency between the nozzle size and resulting stagnation pressure can be explained by analyzing the system in terms of energy. Although the area of the nozzle exit is varied, the area of the plunger remains the same which means the total energy imposed on the fluid for a given driver pressure remains the same irrespective of the exit nozzle area. The only energy losses in the system that could change with nozzle geometry are: wall friction from the changing nozzle wall area, and turbulent energy dissipation as the jet exits into the atmosphere. The CFD stagnation pressure is computed at the nozzle tip, before turbulent losses occur. The difference in wall area for the different nozzles is minimal. Both these conditions together explain why the CFD results show no nozzle size dependence of stagnation pressure. The experimentally measured stagnation pressures also show no consistent trend with nozzle diameter between 130 and 250 μm[4,27].

Simulations are also performed to look at the effect of stand-off distance. The stand-off distance is defined as the gap between the pressure measurement point and the nozzle exit. Although in real practice when the injector is used to administer medication, the nozzle shall come in direct contact with the skin and that the stand-off distance will typically not exist. Nevertheless, it is of interest to analyze if this can represent a source of error in the experimental measurement since it was not possible to have the injector contact the force transducer directly, and to reveal the significance of this effect on the injection performance parameters. Figure 13 illustrates three different gap sizes tested with a 180 μm nozzle and at a driver pressure of 690 kPa and in agreement with the experimental observation[4,27], the numerical results confirms that within the distance from 0 to 15 mm, there is no significant variation in both peak and average stagnation pressure measurement in relation to different gap distances.

The CFD results also confirm that the injection chamber volume does not play a significant role in impacting the peak or average stagnation pressure. The results show that it affects mostly the period over which the damping occurs. Figure 14 illustrates the modeled differences from CFD in the injection time pressure profile for both a 25 mm and 10 mm long chamber length. The CFD results demonstrate an almost identical match in peak pressure and average stagnation pressure; however the shorter column oscillates more frequently about the average stagnation pressure than the longer column. Furthermore, there is also a time shift between the peak stagnation pressures of both column lengths. The longer column requires about 0.2 ms more to reach its peak stagnation pressure than the short column. The time shift can be explained by the fact that the larger volume imparts more energy dissipation shifting the peak of the injection pressure slightly.

More simulations are also performed in order to further explore the notion that injection chamber length has a minimal effect on peak and average pressure. Simulations were carried out using a 129 μm nozzle in conjunction with a 580 kPa driver pressure, and the injection peak and average stagnation pressures were tracked for three different chamber lengths of 10, 25 and 40 mm. Figure 15 illustrates these


(a)
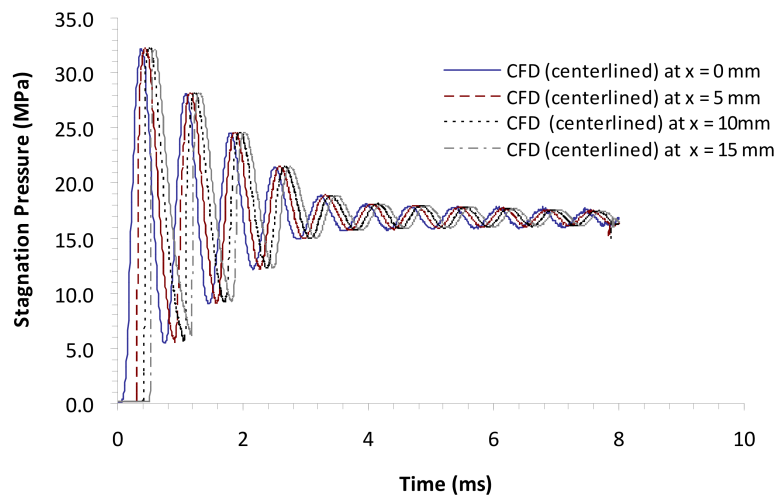
(b)

Fig. 13.   Effect of stand-off distance on stagnation pressure. a) space-averaged CFD value; and b) centerline CFD value.

numerical results, together with the experimental measurement. It shows that the CFD results remain constant as chamber length is increased from 10 mm to 40 mm. Experimentally, there is no specific trend that emerges and the test points are scattered about a constant value. Hence, both results from simulations and experiments illustrate that the injection chamber length has no effect on average stagnation pressure.

As discussed earlier, the accuracy of the numerical solutions of the peak and
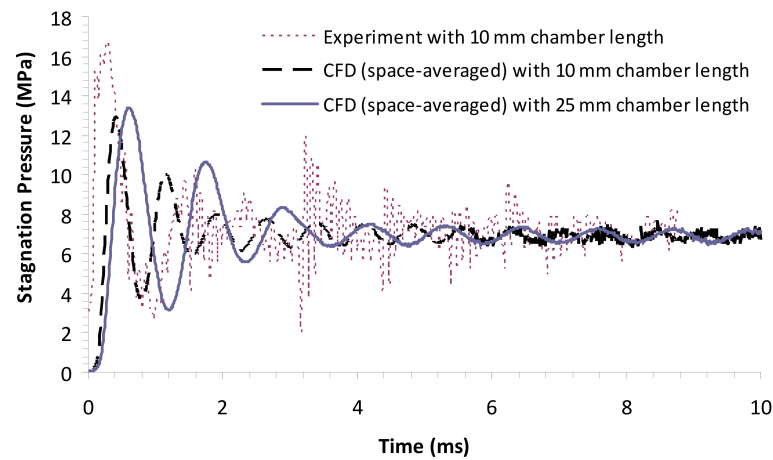
(a)
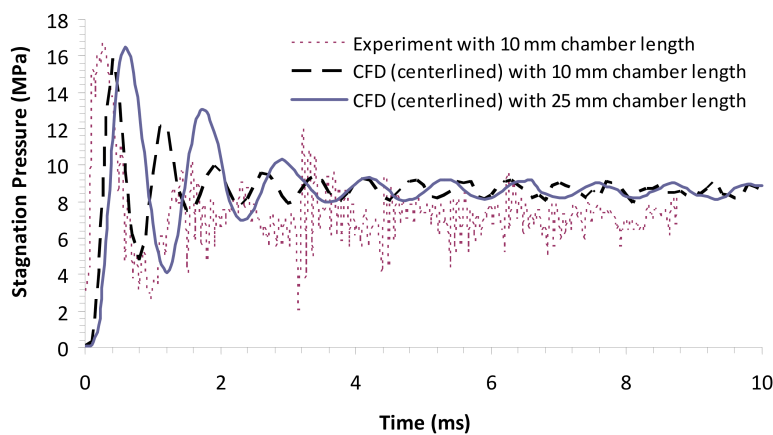
(b)

Fig. 14.   Effect of injection chamber length on stagnation pressure. a) space-averaged CFD value; and b) centerline CFD value.

average stagnation pressures can depend on the modeling of O-ring friction. In addition, the O-ring friction also has an important influence on the settling time for the oscillatory behavior of the time-pressure profile of a given injection. Figure 16 illustrates the modeled behavior of friction; it is possible to see that without friction the model oscillates significantly about an average stagnation pressure, whereas at 50% friction the model settles to an average stagnation pressure more rapidly. Finally, the numerical model behavior with friction settles to an average value within
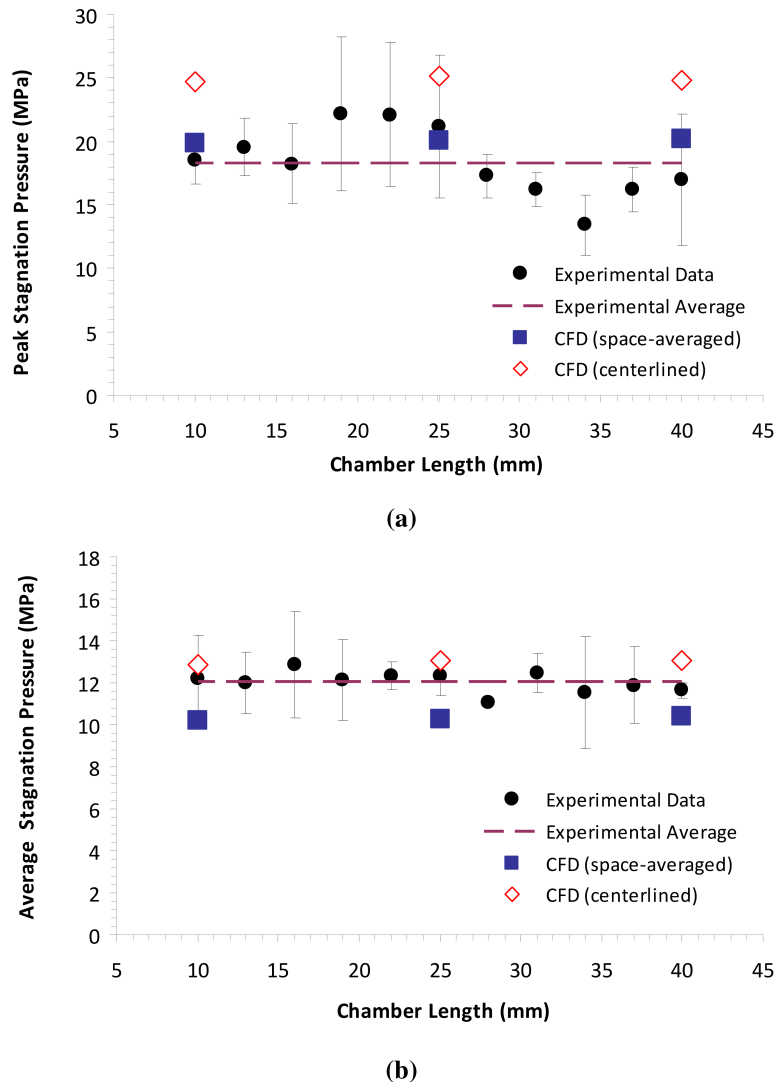

(a)

(b)

Fig. 15.   a) Peak and b) average stagnation pressures obtained for different chamber lengths of the injector with a 129 μm nozzle and $p_D = 580$ kPa.

approximately the first 2 ms of the injection. The peak and average stagnation values are slightly lower than those predicted without O-ring friction.
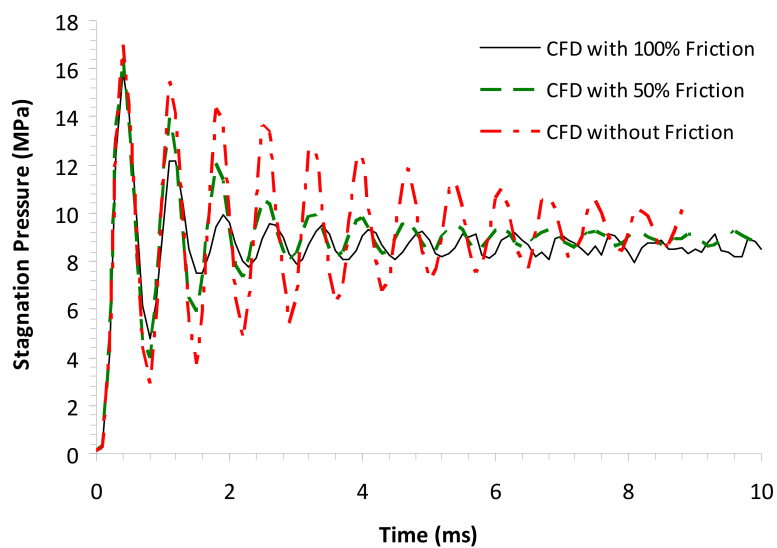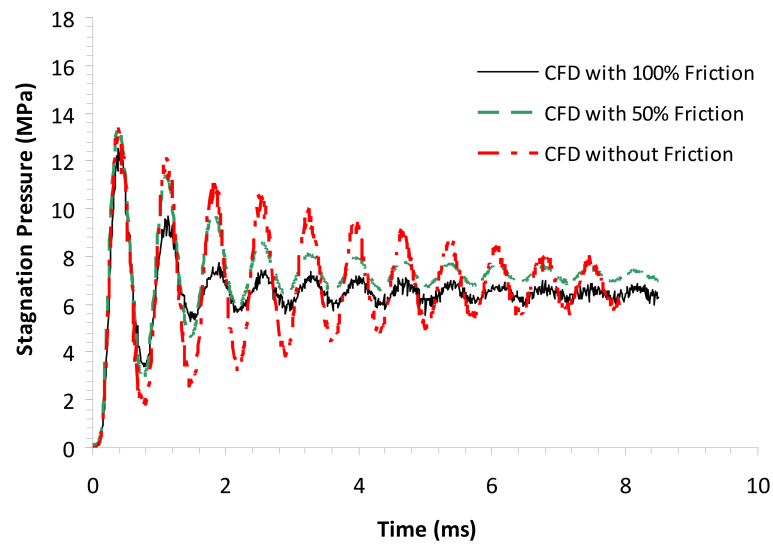

(a)

(b)

Fig. 16.   Effect of friction on the stagnation pressure. a) space-averaged CFD value; and b) centerline CFD value.

4. Conclusion

Using a combined LES/VOF technique with dynamic mesh and moving boundary method, made it possible to successfully simulate the behavior and performance characteristics of an air-powered needle free injector. Numerical results for stagnation pressure, one of the key performance parameters for needle free liquid injectors, are compared with experimental measurements; and the general experimental observations agree very closely with the numerical model developed throughout this study. The CFD model makes it possible to analyze which parameters among driver pressure, nozzle diameter, liquid column length and frictional losses most significantly impact the peak and average stagnation pressures of the jet exiting the air-powered needle free liquid injector and to obtain an optimal design of this biomedical engineering device. The CFD model also agrees very closely with similar experimental studies discussed in Portaro and Ng[4,27]. CFD results demonstrate that as the driver pressure increased both the peak and average stagnation pressure increased almost linearly within the operating range considered. Varying the injection nozzle diameter, whilst keeping the driver pressure constant does not have any significant impact on the peak or average stagnation pressure. The chamber length and the stand-off distance were varied, and no significant influence is found on peak or average stagnation pressure. The validated numerical results obtained in this work mean this numerical model can be readily used in future research, to further explore the relationships between various injector design parameters and improve the injectors effectiveness in delivering an injection.

References

1. Mitragotri S, Immunization without needles, *Nature Rev. Immunology* **5**:905–917, 2005.
2. Mitragotri S, Current status and future prospects of needle free liquid jet injectors, *Nature Rev. Drug Discovery* **5**:543–548, 2006.
3. Kendall MA, Needle free vaccine injection, in *Handbook of experimental pharmacology*, Springer-Verlag, Berlin, pp. 194–215, 2010.
4. Portaro R, Ng HD, Experimental analysis of the performance of an air-powered needle-free liquid jet injector, in *Proc. 35th Int. Conf. IEEE Eng. Medicine & Biology Soc.*, Osaka, Japan, 2013.
5. Hingson RA, Davis HS, Rosen M, Historical development of jet injection and envisioned uses in mass immunization and mass therapy based upon 2 decades experience, *Mil. Med.* **128**:516–524, 1963.
6. Wijsmuller G, Snider Jr DE, Skin testing: A comparison of the jet injector with the mantoux method, *Am. Rev. Respir. Dis.* **112**:789–798, 1975.

7. Schneider U, Birnbacher R, Schober E, Painfulness of needle and jet injection in childern with diabetes mellitus, *Eur. J. Pediatr.* **153**:409–410, 1994.

8. Schramm JR, Mitragotri S, Transdermal drug delivery by jet injectors: Energetics of jet formation and penetration, *Pharm. Res.* **19**:1673–1679, 2002.

9. Schramm-Baxter J, Mitragotri S, Investigations of needle-free jet injections, in *Proc. 26th Annual Int. Conf. IEEE EMBS*, San Francisco, USA, 3543–3546, 2004.

10. Schramm-Baxter J, Mitragotri S, Needle-free jet injections: dependence of jet penetration and dispersion in the skin on jet power, *J. Control. Release*, **97**:527–535, 2004.

11. Schramm-Baxter J, Katrencik J, Mitragotri S, Jet injection into polyacrylamide gels: investigation of jet injection mechanics, *J. Biomech.* **37**:1181–1188, 2004.

12. Baker AB, Sanders JE, Fluid mechanics analysis of a spring- loaded jet injector, *IEEE Trans. Biomed. Eng.* **26**(2):235–242, 1999.

13. Shergold OA, Fleck NA, King TS, The penetration of a soft solid by a liquid jet, with application to the administration of a needle-free injection, *J. Biomech.* **39**:2593–2602, 2006.

14. Chen K, Zhou H, Li J, Cheng GJ, A model on liquid penetration into soft material with application to needle-free jet injection, *Int. ASME J. Biomech. Eng.* **132**(10):101005, 2010.

15. Taberner AJ, Ball NB, Hogan NC, Hunter IW, A portable needle-free jet injector based on a custom high power-density voice-coil actuator, in *Proc. 28th Annual Int. Conf. IEEE EMBS*, New York City, USA, 2531–2534, 2006.

16. Taberner A, Hogan NC, Hunter IW, Needle-free jet injection using real-time controlled linear Lorentz-force actuators, *Med. Eng. Phys.* **34**(9):1228–1235, 2012.

17. Hemond BD, Wendell DM, Hogan NC, Taberner AJ, Hunter IW, Lorentz-force actuated autoloading needle-free injector, in *Proc. 28th Annual Int. Conf. IEEE EMBS*, New York City, USA, pp. 2318–2321, 2006.

18. Stachowiak JC, von Muhlen MG, Li TH, Piezoelectric control of needle free transdermal drug delivery, *J. Control. Release* **124**:88–97, 2007.

19. Mohanty C, Mannavathy CD, Srikanth D, Tabassum R, Needle free drug delivery systems: A review, *Int. J. Pharmaceutical Research Development (IJPRD)* **3**(7):7–15, 2011.

20. Kendall MAF (2002) The delivery of particulate vaccines and drugs to human skin with a practical, hand-held shock tube-based system. Shock Waves 12(1):22-30.

21. Liu Y, Kendall MAF (2004) Numerical study of a transient gas and microparticle flow in a high-speed needle-free ballistic particulate vaccine delivery system. J. Mech. Med. Biol. 4(4):559-578

22. Liu Y, Kendall MAF (2005) Numerical analysis of gas and micro-particle interactions in a hand-held shock-tube device. Biomedical Microdevices 8(4):341-351.

23. Liu Y (2006) Physical-mathematical modelling of fluid and particle transportation for DNA vaccination. Int. J. Eng. Sci. 44(15-16):1037-1049.

24. Liu Y (2007) The use of miniature supersonic nozzles for microparticle acceleration: a numerical study. IEEE Trans. Biomed. Eng. 54(10):1814-1821.

25. Pianthong K, Seehanam W, Sittiwong W, Milton B (2011) Injection characteristics of liquid jet from a needle free injection device in the tissue stimulant. The 2nd TSME International Conference on Mechanical Engineering, 19-21 October, 2011, Krabi.

26. OpenCFD, OpenFOAM, The Open Source CFD Toolbox, User Guide, *OpenCFD Ltd*, 2013.

27. Portaro R, Ng HD, Experiments and modeling of air-powered needle force liquid injectors, *Accepted for J. Med. Biol. Eng. (In press)*, 2013.

28. Chen K, Zhou H, Li J, Cheng GJ, Stagnation pressure in liquid needle-free injection: modeling and experimental validation, *Int. Drug Deliv. Letters* **1**:97–104, 2011.
29. Darcoid Norcal Seals, O-ring load per linear inch of seal empirical chart, *http://www.darcoid.com/images/uploads/pdfs/empiricalcharts*
30. Guang TH, Wang DT, *Operation Manual of Sealing Components*, Mech. Ind. Press, Beijing, 1994.
31. Barton IE, Comparison of SIMPLE- and PISO-type algorithms for transient flows, *Int. J. Numer. Meth. Fluids* **26**:459–483, 1998.
32. Ferziger J. Peric M, *Computational Methods for Fluid Dynamics, 2nd edition*, Springer, Berlin, 1999.
33. Arora A, Hakim I, Baxter J, Rathnasingham R, Srinivasan R, Fletcher D, Mitragotri S, Needle free delivery of macromolecules across the skin by nanolitre-volume pulsed microjets, *Proc. Nat. Acad. Sci.* **104**(11):4255–4260, 2007.